Inorganic Chemistry

pubs.acs.org/IC Article

ThMnPnN (Pn = P, As): Synthesis, Structure, and Chemical Pressure Effects

Fuxiang Zhang, Baizhuo Li, Qingyong Ren, Huican Mao, Yuanhua Xia, Bingfeng Hu, Zichen Liu, Zhicheng Wang, Yeting Shao, Zhifa Feng, Shugang Tan, Yuping Sun, Zhi Ren, Qiang Jing, Bo Liu, Huiqian Luo, Jie Ma, Yuxue Mei,* Cao Wang,* and Guang-Han Cao

Cite This: *Inorg. Chem.* 2020, 59, 2937−2944 Read Online

ACCESS | Metrics & More | Article Recommendations | Supporting Information

ABSTRACT: Mn-based ZrCuSiAs-type pnictides ThMnPnN (Pn = P, As) containing PbO-type Th_2N_2 layers were synthesized. The crystal and magnetic structures are determined using X-ray and neutron powder diffraction. While neutron diffraction indicates a C-type antiferromagnetic state at 300 K, the temperature dependence of the magnetic susceptibility shows cusps at 36 and 52 K respectively for ThMnPN and ThMnAsN. The susceptibility cusps are ascribed to a spontaneous antiferromagnetic-to-antiferromagnetic transition for Mn^{2+} moments, which is observed for the first time in Mn-based ZrCuSiAs-type compounds. In addition, measurements of the resistivity and specific heat suggest an abnormal increase in the density of states at the Fermi energy. The result is discussed in terms of the internal chemical pressure effect.

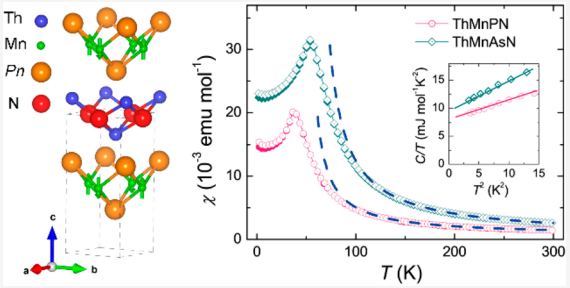

INTRODUCTION

The prototype compound of iron-based superconductors LaFeAsO structurally consists of alternating stacks of PbO-type $[La_2O_2]^{2+}$ and anti-PbO-type $[Fe_2As_2]^{2-}$ layers.[1] This ZrCuSiAs-type (1111) structure is so adaptable that for every crystallographic site there are a number of candidate elements that can make it stable.[2−6] For instance, the $[La_2O_2]^{2+}$ layer can be replaced by $[Ln_2O_2]^{2+}$ (Ln stands for lanthanides),[4−6] $[An_2O_2]^{2+}$ (An = Np, Pu),[7,8] $[Ae_2F_2]^{2+}$ (Ae = alkali-earth metal or Eu),[9,10] and $[Ca_2H_2]^{2+}$.[11] As for the $[Fe_2As_2]^{2-}$ layer, there are also tens of the alternatives, denoted as $[T_2Pn_2]^{2-}$, where T and Pn represent transition metals and pnictogen elements, respectively. In the numerous 1111 compounds, the $[T_2Pn_2]^{2-}$ layers play the key role in determining the diverse physical properties including metallic antiferromagnetism (AFM) in LnCrAsO,[12] insulating AFM in LaMnPnO,[13] high-temperature superconductivity in $LaFeAsO_{1-x}F_x$,[1] itinerant ferromagnetism (FM) in LnCoPnO,[14−17] and Pauli paramagnetism (PM) with low-temperature superconductivity in LaNiPnO.[18,19]

Mn-based 1111 compounds are of special interest for their insulating AFM, akin to that of the parent compounds of cuprate high-temperature superconductors. The Néel temperatures (T_N) of LnMnPnO are between 230 and 360 K, and the ordered magnetic moment for Mn^{2+} spins is in the range of 3.2−4.2 μ_B.[13] The Mn moments can be understood in terms of the half-filling of 3d orbitals, which maximizes Hund's coupling. Below the T_N values, the moments on Mn^{2+} align along the *c* axis. In the cases of NdMnAsO, PrMnSbO, and CeMnAsO, reorientation of the Mn^{2+} moment onto the *ab* plane is observed at lower temperatures, accompanied by antiferromagnetic ordering of the local moment on Ln^{3+}.[20−22] Most of the Mn-based 1111 compounds exhibit an insulating behavior with a typical room-temperature resistivity of about 10^4 Ω·cm.[23−26] Upon Sr/La substitution in LaMnAsO, the system changes to an antiferromagnetic metal.[23] It is reported that the AFM in LaMnPO can also be suppressed under high pressures, yet no superconductivity was observed above 1.5 K.[27,28]

Recently, we discovered a new 1111-type Fe-based compound ThFeAsN that superconducts at 30 K without external chemical doping.[29,30] Although theoretical calculations suggest a striped antiferromagnetic ground state,[31] no magnetic ordering of the Fe moments was found down to 2.0 K.[32−35] We also synthesized a Ni-based isomorphic compound ThNiAsN, which shows the highest superconducting transition temperature T_c among the Ni-based 1111-type family.[36] The abnormal behavior of ThFeAsN and ThNiAsN is attributed to the internal chemical pressure from the $[Th_2N_2]^{2+}$ layers.[29,36] Thus, it is of interest to investigate the Mn-based 1111-type pnictides with $[Th_2N_2]^{2+}$ layers.

In this paper, we report the synthesis, structure, and physical properties of ThMnPnN (Pn = P, As). The neutron powder

Received: November 9, 2019
Published: February 17, 2020

https://dx.doi.org/10.1021/acs.inorgchem.9b03294
Inorg. Chem. 2020, 59, 2937−2944

diffraction indicates that the antiferromagnetic states are established at room temperature; nevertheless, the magnetic susceptibility still exhibits a Curie–Weiss-like behavior below 300 K. There are cusps at 36 K (ThMnPN) and 52 K (ThMnAsN) on the $\chi-T$ curves, suggestive of the second spontaneous antiferromagnetic phase transition for the Mn^{2+} moments. In addition, the transport measurement indicates a significant enhancement of the conductivity, consistent with the nonzero Sommerfeld coefficients obtained from the heat-capacity measurement. The unique properties of ThMnPnN are discussed in terms of the internal chemical pressure effect.

EXPERIMENTAL SECTION

Caution! *All of the materials and compounds containing Th are radioactive, including ThO_2, Th, Th_3N_4, and ThMnPnN. Precautions with suitable care and protection for handling such substances were followed.*

Polycrystalline samples of ThMnPnN were synthesized by a conventional solid-state reaction using the powdered chemicals of Th_3N_4 and MnAs (or MnP). The Th metal ingot and Th_3N_4 powders were obtained as described elsewhere.[29] The binary products MnAs and MnP were prepared using the powder of As (99.999%), red P (99.999%), and Mn (99.99%) at 973 K in evacuated fused-silica tubes. A stoichiometric mixture of Th_3N_4 and MnAs/MnP (Th:Mn:Pn = 1:1:1) was cold-pressed into pellets and loaded into boron nitride crucibles (the crucible was heated to 773 K overnight in air to remove absorbed water in advance). Then the crucibles were sealed in evacuated fused-silica tubes and heated at 1373 K for 60 h. The solid-state reaction was repeated with intermediate regrinding.

Powder X-ray diffraction (XRD) was carried out at room temperature on a PANalytical X-ray diffractometer (model EMPYREAN) with monochromatic Cu $K\alpha_1$ radiation. The crystal structure data were obtained by Rietveld refinement using the step-scan XRD data with $20° \leq 2\theta \leq 120°$ for all of the samples. Neutron powder diffraction experiments were carried out on the High-Resolution Neutron Diffractometer at the Key Laboratory of Neutron Physics, Institute of Nuclear Physics and Chemistry, China Academy of Engineering Physics. About 5 g of high-purity sample was used in the neutron diffraction for both compounds (sealed in a V can). The wavelength of the neutron was $\lambda = 1.8846$ Å. The scattering data were collected at 4 and 300 K by covering the scattering angle in the range $2\theta = 8–145°$. The XRD and neutron diffraction patterns were refined with the Rietveld method using the programs *RIETAN-FP* and *FullProf*,[37] respectively. The structural parameters were obtained by assuming that the occupancy was the same as the chemical composition.[33] Magnetic measurements were performed on a Quantum Design Magnetic Property Measurement System (MPMS-XL5). The temperature-dependent resistivity was measured using a standard four-terminal method on a Cryogenic Mini-CFM measurement system equipped with a Keithley 2400 digital sourcemeter and a Keithley 2182 nanovoltmeter. Measurement of the specific heat was performed on a Quantum Design Physical Property Measurement System (PPMS-9) using a thermal relaxation method.

RESULTS AND DISCUSSION

Figure 1 shows the powder XRD patterns and their Rietveld refinement profiles for ThMnPnN (Pn = P, As) polycrystalline samples. No extra XRD peaks can be observed in the pattern, indicating that our samples are phase-pure. Table 1 lists the refined crystal-structure parameters. Generally speaking, the unit cell tends to expand in all three dimensions when an atom in the structure is substituted with a bigger one, and the lattice expansion is anisotropic in most cases. In a comparison of the lattice parameters of ThMnPN and ThMnAsN, the expansions due to the replacement of P for As are 1.28% (a axis) and 3.03% (c axis), respectively. This is associated with the detailed

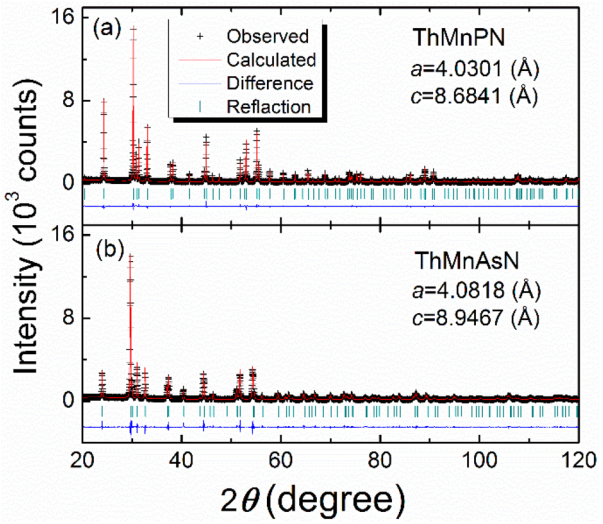

Figure 1. Rietveld refinement profiles of the powder XRD for ThMnPN (a) and ThMnAsN (b).

Table 1. Crystallographic Parameters for ThMnPnN Determined by Rietveld Refinement of Powder XRD at 300 K[a]

			ThMnPN		ThMnAsN
space group			*P4/nmm*		*P4/nmm*
a (Å)			4.0301(3)		4.0818(7)
c (Å)			8.6841(7)		8.947(2)
R_{wp} (%)			6.08		8.30
R_p (%)			4.82		6.33
χ^2			1.06		2.11
H_{Pn} (Å)			1.3978		1.5472
Pn–Mn–Pn angle (deg)			110.49		105.68
atom	Wyckoff	x	y	z	U_{iso}
			ThMnPN		
Th	2c	0.25	0.25	0.13586(5)	0.0021(1)
Mn	2b	0.75	0.25	0.5	0.0041(5)
P	2c	0.25	0.25	0.6610(4)	0.0051(7)
N	2a	0.75	0.25	0	0.008(3)
			ThMnAsN		
Th	2c	0.25	0.25	0.13091(8)	0.0015(2)
Mn	2b	0.75	0.25	0.5	0.0073(9)
As	2c	0.25	0.25	0.6729 (2)	0.0037(7)
N	2a	0.75	0.25	0	0.014(5)

[a] H_{Pn} represents the pnictogen height relative to the Mn plane.

structure of the MnPn block layers, characterized by the change of the Pn height as well as the 2-fold Pn–Mn–Pn bond angles. Table 2 compares the cell parameters of the related 1111-type pnictides containing Th_2N_2 or La_2O_2 layers. For the Fe-based pnictides LaFeAsO and ThFeAsN, while their a axes are almost identical, the c axis of ThFeAsN is distinctly shorter than that of LaFeAsO, suggesting the existence of an additional uniaxial chemical pressure along the c axis in ThFeAsN.[29] Similar built-in uniaxial chemical pressures were also seen in ThNiAsN and ThMnPN, according to the axial ratio c/a. The cell volumes for ThNiAsN and ThMnPN decrease by 4.45% and 3.15% (compared with LaNiAsO and LaMnPO), respectively. Thus, the relative chemical pressures in ThNiAsN and ThMnPN are even higher than that in ThFeAsN (2.38%, compared with LaFeAsO). As for ThMnAsN, although the

https://dx.doi.org/10.1021/acs.inorgchem.9b03294
Inorg. Chem. 2020, 59, 2937–2944

Table 2. Lattice Parameters of 1111-Type Pnictides Containing Th_2N_2 or La_2O_2 Layers[a]

compound	a (Å)	c (Å)	c/a	volume (Å^3)	$(V_{Th} - V_{La})/V_{La}$ (%)
La**FeAs**O[1]	4.0355	8.7393	2.166	142.32	−2.38
Th**FeAs**N[25]	4.0367	8.5262	2.112	138.93	
La**NiAs**O[18]	4.1231	8.1885	1.986	139.20	−4.45
Th**NiAs**N[35]	4.0804	7.9888	1.958	133.01	
La**MnP**O[23]	4.0579	8.8434	2.189	145.62	−3.15
Th**MnP**N	4.0301	8.6841	2.155	141.04	
La**MnAs**O[13]	4.1200	9.0462	2.196	153.55	−2.92
Th**MnAs**N	4.0818	8.947	2.192	149.07	

[a] V_{La} and V_{Th} respectively represent the unit cell volumes of La- and Th-based 1111 compounds.

shrinkage of the cell volume reaches 2.92%, the axial ratios of LaMnAsO and ThMnAsN are very similar, which means that the chemical pressure in ThMnAsN is more isotropic.

Figure 2 shows the neutron powder diffraction patterns and the structure model employed in the refinement for both of the compounds. The data are collected at 300 and 4 K for comparison. Table 3 summarizes refined structural and magnetic parameters of the neutron powder diffraction. For the room temperature diffraction data, the obtained structural parameters agree with those obtained from the XRD measurements, with the differences of less than 0.5‰. For

Table 3. Crystallographic Data of ThMnPnN from Refinement of the Neutron Powder Diffraction Data at 300 and 4 K[a]

	ThMnPN		ThMnAsN	
	300 K	4 K	300 K	4 K
space group	*P*4/*nmm*	*P*4/*nmm*	*P*4/*nmm*	*P*4/*nmm*
a (Å)	4.0318(2)	4.0259(1)	4.0833(2)	4.0764(2)
c (Å)	8.6878(5)	8.6736(4)	8.9484(5)	8.9298(5)
R_{wp} (%)	7.22	7.57	6.15	5.60
z(Th)	0.1358(4)	0.1359(4)	0.1300(5)	0.1301(4)
z(P/As)	0.6621(8)	0.6616(9)	0.6705(7)	0.6727(7)
B_{iso}(Th)	1.47(10)	0.98(14)	1.60(14)	1.17(15)
B_{iso}(Mn)	1.27(19)	0.72(22)	1.41(22)	1.11(22)
B_{iso}(P/As)	1.56(16)	1.05(20)	1.62(16)	1.06(16)
B_{iso}(N)	1.14(13)	0.97(16)	0.83(15)	0.70(16)
Mn moment (μ_B)	2.69(9)	3.60(10)	2.30(11)	3.41(8)

[a] During the refinement, the occupancy of all of the atomic sites is fixed to 1.0.

the data collected at 4 K, the Rietveld refinement gives the lattice parameters of a = 4.0259(1) Å and c = 8.6736(4) Å for ThMnPN and a = 4.0764(2) Å and c = 8.9298(5) Å for ThMnAsN. The magnetic peaks can be indexed with a propagation vector $\boldsymbol{k}$ = (0, 0, 0). Irreducible representation analysis based on the crystal structure demonstrates a C-type antiferromagnetic ordering, meaning the coupling between the

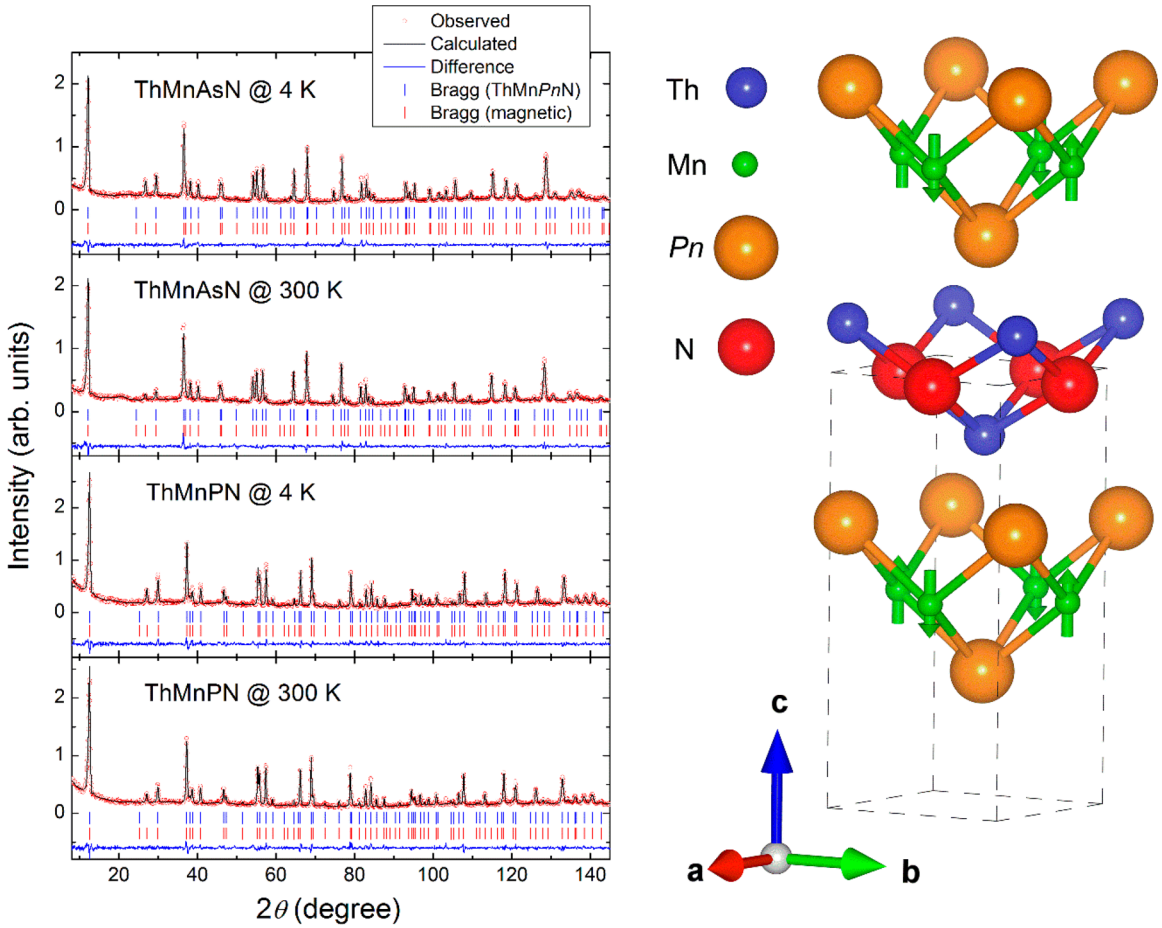

Figure 2. Left: Rietveld refinement of the neutron powder diffraction data. Right: Structure model employed in the refinement. The arrow indicates the direction of the magnetic moment giving the best results in the refinement of neutron powder diffraction.

https://dx.doi.org/10.1021/acs.inorgchem.9b03294
Inorg. Chem. 2020, 59, 2937−2944

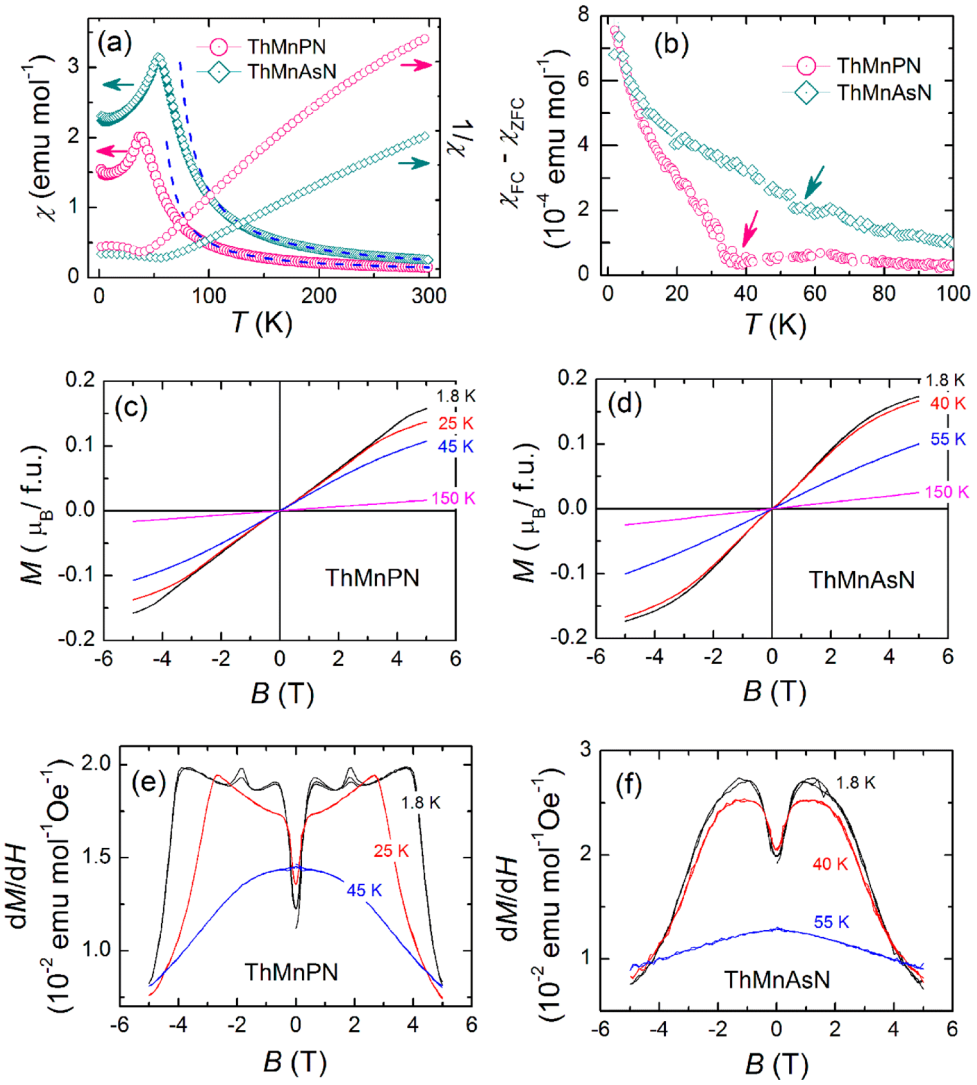

Figure 3. (a) Temperature dependence of the magnetic and inverse magnetic susceptibilities ($1/\chi$) for ThMnPN and ThMnAsN. The dashed line is a fit to the extended Curie–Weiss law: $\chi(T) = \chi_0 + C/(T - \theta)$. Both ZFC and FC were performed in a static field of 1000 Oe. (b) Enlarged view of $\chi_{FC}-\chi_{ZFC}$ against the temperature for both compounds to show bifurcation below the T^* values. (c and d) Isothermal magnetization of ThMnPN and ThMnAsN. (e and f) Derivative of magnetization with respect to the magnetic field.

nearest-neighbor Mn^{2+} ions in the *ab* plane are antiferromagnetic, while ferromagnetic alignments are adopted between the adjacent $[Mn_2Pn_2]^{2-}$ layers along the *c* axis. During the refinement, the best agreement is achieved when the Mn^{2+} moments are aligned parallel to the *c* axis. However, incorporating the magnetic moment component in the *ab* plane into the refinement does not cause a significant increase in the *R* factors (see the details in the Supporting Information). It is difficult to distinguish the exact direction of the ordering magnetic moment base on the current neutron powder diffraction data. Here, the C-type antiferromagnetic structure with magnetic moments directed along the *c* axis was adopted, as depicted in Figure 2, and is similar to most of the MnPn-layer-based compounds.[13] The magnetic moments at 4 K are determined as 3.60(10) and 3.41(8) μ_B/Mn for ThMnPN and ThMnAsN, respectively, which are close to those of other 1111-type Mn-based materials.[13] This moment reduction (from the full moment of $gS = 5$ μ_B) has been attributed to valence fluctuations.[28]

Figure 3 shows the magnetic measurement results of the two samples. As shown in Figure 3a, the room-temperature susceptibilities of ThMnPN and ThMnAsN are 1.66×10^{-3} and 2.69×10^{-3} emu mol^{-1}, respectively. Upon cooling, the susceptibility gradually increases until it reaches the T^* values (T^* = 36 and 52 K mark the cusps for ThMnPN and ThMnAsN, respectively). Below the T^* values, the susceptibility decreases with decreasing temperature, and slight bifurcations between the zero-field-cooling (ZFC) and field-cooling (FC) curves are observed, which can be seen more clearly in Figure 3b. Given the closed electronic shell for the Th^{4+} ions, the susceptibility cusps at T^* values should still be contributed from the magnetism of Mn atoms. Because the antiferromagnetic ordering of the Mn^{2+} moment is already established at 300 K, the cusps suggest a successive magnetic transition associated with the Mn moment, although the corresponding change in the magnetic structure was not detected by neutron diffraction. We note that a spin reorientation for the Mn^{2+} moment was observed at low temperatures in NdMnAsO, PrMnSbO, and CeMnAsO,[20−22] in which the Mn moment flops onto the *ab* plane accompanied by the long-range antiferromagnetic ordering of the Ln^{3+} moments. For LaMnAsO, where there is no magnetic moment

https://dx.doi.org/10.1021/acs.inorgchem.9b03294
Inorg. Chem. 2020, 59, 2937−2944

at the La site, such a spin reorientation was absent.[13] In this context, one does not expect the LnMnAsO-like spin-reorientation transition in ThMnPnN because Th^{4+} is also nonmagnetic. Indeed, our neutron diffraction data at 4 K do not favor the Mn moment lying in the *ab* plane (see Table S1).

Another surprising phenomenon is that the susceptibility above the T^* values decreases with increasing temperature and can be fitted with the extended Curie–Weiss law $\chi(T) = \chi_0 + C/(T - \theta)$ over a temperature region of 150–300 K. The derived parameters are $\chi_0 = 3.3 \times 10^{-4}$ emu mol^{-1}, $C = 0.231$ emu K mol^{-1}, and $\theta = 48.7$ K for ThMnPN and $\chi_0 = 5.2 \times 10^{-4}$ emu mol^{-1}, $C = 0.493$ emu K mol^{-1}, and $\theta = 55.8$ K for ThMnAsN. The positive χ_0 and θ values suggest Pauli PM with ferromagnetic interaction. The Curie constants correspond to "residual" effective magnetic moments of 1.36 and 1.99 μ_B per formula unit for ThMnPN and ThMnAsN, respectively. We note that, although similar Curie–Weiss-like behaviors in the antiferromagnetic state were reported in NdMnAsO and PrMnSbO,[20,22] the PM was associated with the local moment of Ln^{3+} rather than Mn^{2+}. As a comparison, there is no such Curie–Weiss-like PM in the antiferromagnetic states of LaCrAsO[12] and $BaMn_2As_2$.[38] Thus, the PM above the T^* values in ThMnPnN suggests that only a part of the Mn^{2+} moment has been arranged antiferromagnetically below the Néel temperature, leaving the rest of the moments in a paramagnetic or disordered state until the sample is cooled to below the T^* values. This phenomenon has been reported in the $Nd_{1-x}Sr_xMnAsO$ system, where the antiferromagnetically ordered moment of Mn^{2+} sharply increases from 2.8 to 3.6 μ_B at 24 K.[39] Supposing that the Mn^{2+} ion in ThMnPnN behaves similarly to those in $Nd_{1-x}Sr_xMnAsO$, the susceptibility cusps observed at the T^* values should be ascribed to a further antiferromagnetic transition for the previous paramagnetic/disordered part of the Mn^{2+} moments below T_N.

Parts c and d of Figure 3 show M–H curves at selected temperatures for both of the compounds. At first glance, for all of the selected temperatures, the magnetization increases linearly with the magnetic field in the low-field region. When the derivative of magnetization (dM/dH) is plotted as a function of the magnetic field (Figure 3e,f), one can see something different. For temperatures higher than the T^* values, dM/dH shows a broad hump over the entire field range, exhibiting an ordinary magnetization behavior. At temperatures lower than the T^* values, however, dM/dH shows a distinct valley in the low-field area and an abrupt decrease in the high-field one, denoting a weak metamagnetic transition. A possible explanation for the metamagnetism is that the ordered moments below the T^* values may exhibit instability in the external magnetic field because there is no magnetic coupling between Mn^{2+} and Th^{4+}. This is also consistent with the slight bifurcations between the ZFC and FC χ–T curves.

The temperature-dependent electrical resistivity of ThMn*Pn*N is plotted in Figure 4. For Pn = P (Figure 4a), the resistivity at 300 K is 0.0328 Ω·cm, which is in sharp contrast to that of LaMnPO (~10^3 Ω·cm).[26,27] Furthermore, the resistivity decreases upon cooling and reaches its minimum (0.0226 Ω·cm) at 78 K. There is a slope change at 36 K, coincident with the cusp observed in the χ–T curve. At lower temperatures, the resistivity gradually increases. For Pn = As (Figure 4b), the room temperature resistivity is 0.134 Ω·cm, which is about 4 orders of magnitude lower than that of LaMnAsO.[23,24] Upon cooling, the resistivity shows semiconducting behavior. No resistivity anomaly shows up around

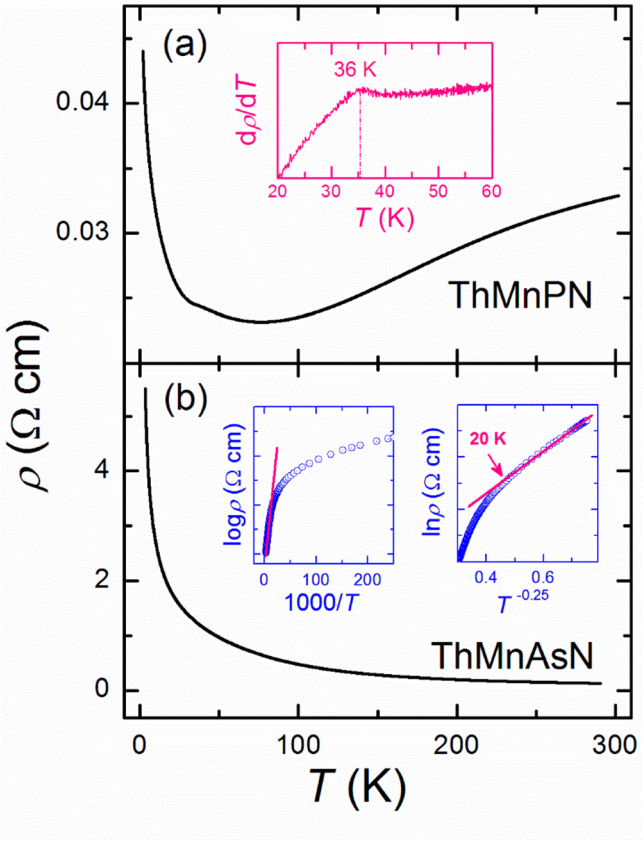

Figure 4. (a) ρ–T data for ThMnPN. The inset shows the plot of $d\rho/dT$ versus T for ThMnPN to show the anomaly clearly. (b) ρ–T data for ThMnAsN. Left inset: Plot of $d\rho/dT$ versus T. Right inset: Arrhenius plot of the ρ–T data.

the T^* value of ThMnAsN. We fit the high-temperature data (200–285 K) using the Arrhenius equation $\rho = \rho_0 \exp(E_a/k_BT)$, where ρ_0 refers to a prefactor and k_B is Boltzmann's constant (left inset of Figure 4b). The activation energy (E_a) is extracted to be 10 meV, which is much lower than those of the isostructural Mn-based compounds.[23,24] Considering the single-phase nature of the samples, it is reasonable to ascribe the abnormal low resistivity and low E_a to the intrinsic properties. This implies that a few charge carriers have existed in the system, probably because of the inevitable non-stoichiometry[33] and/or the instability of the 3d electrons in the system.[28] At low temperatures, the measured resistivity is much lower than that predicted by the Arrhenius equation. So, we plot the logarithm of the resistivity (ln ρ) versus $T^{-1/4}$ according to the three-dimensional Mott variable-range hopping (VRH) mechanism $\rho = \rho_0 \exp(T_0/T)^{1/4}$ in the right inset of Figure 4b. Below 20 K, the ln ρ value is proportional to $T^{-1/4}$ and yields the localization temperature $T_0 = 199$ K. As a comparison, the low-temperature VRH T_0 values for both NdMnAsO and $PrMnAsO_{0.95}F_{0.05}$ reach as high as ~2×10^5 K.[40,41] We note that T_0 represents the degree of disorder and can be written as $T_0 = \lambda\alpha^3/k_BN_{EF}$, where λ is a dimensionless constant, α is the localization parameter that reflects the potential landscape surrounding the hopping sites, and N_{EF} is the localized density of states near the Fermi level. Supposing that both ThMnAsN and NdMnAsO share a similar α factor, the reduced T_0 indicates a significant increase of N_{EF} in ThMnAsN.

https://dx.doi.org/10.1021/acs.inorgchem.9b03294
Inorg. Chem. 2020, 59, 2937–2944

The temperature dependence of the specific heat is given in Figure 5. The high-temperature data are not far from the value

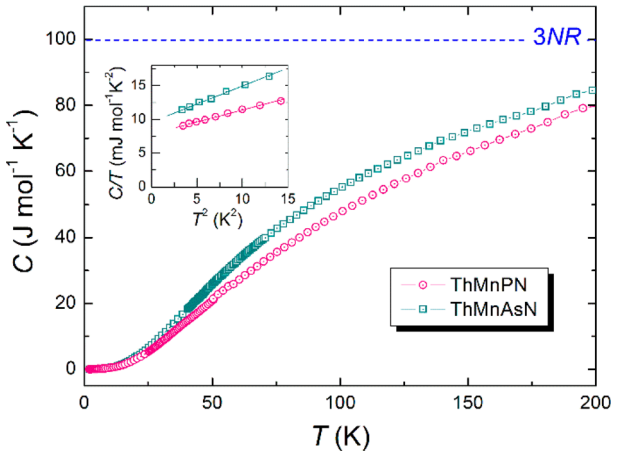

Figure 5. Temperature-dependent specific heat for ThMnPN and ThMnAsN. The inset gives the low-temperature part of the fitted data using the equation $C_{fitted} = \gamma T + \beta T^3$.

of 3*NR* expected from the Dulong–Petit law. No anomaly can be observed around the T^* values, suggesting that the entropy change associated with the low-temperature antiferromagnetic transition is negligibly small. Supposing that the low-temperature specific heat can be written as $C = \gamma T + \beta T^3$, we fit the data below 20 K, where C/T is approximately proportional to T^2. The derived γ is 8.11 mJ mol^{-1} K^{-2} and 9.62 mJ mol^{-1} K^{-2} for ThMnPN and ThMnAsN, respectively. In general, the γ value of an insulator or a semiconductor is nearly zero because of the null density of states at the Fermi energy. For instance, the γ value of NdMnAsO is only 1.2 mJ mol^{-1} K^{-2}.[20] Here the appreciably large γ indicates the nonzero density of states at the Fermi energy, which is consistent with the $\rho-T$ data. Also, the γ value can be related to the Pauli paramagnetic susceptibility (χ_p) by $\gamma = \pi^2 N_A k_B^2 N_{EF}/3$ and $\chi_p = \mu_B^2 N_A N_{EF}$, where N_A is Avogadro's constant and μ_B is the Bohr magneton. This yields χ_p of 1.11×10^{-4} and 1.32×10^{-4} emu mol^{-1} for ThMnPN and ThMnAsN, respectively. The χ_p values are of the same order of magnitude as the χ_0 values derived from the $\chi-T$ plots, although they are not precisely consistent with each other. The inconsistency can be ascribed to impurity effects.

Now let us discuss the unique physical properties of ThMnPnN. As we mentioned above, like all other 1111-type compounds containing Th_2N_2 block layers, both ThMnPN and ThMnAsN bear internal chemical pressure. Comparing the chemical pressure effects with those of the physical pressure, one can find the similarities. Taking LaMnPO, for example,[27,28] as the physical pressure increases, the material is driven from an insulator to a metal (manifested by metallic resistivity behavior) and the room temperature resistivity decreases by 4 orders of magnitude at ~20 GPa.[27] Also, the E_a value derived from the $\rho-T$ curve decreases with increasing pressure and reaches 10 meV at ~22 GPa.[27] Thus, both the E_a value and the room temperature resistivity of LaMnPO at ~20 GPa coincide with those of ThMnPN under ambient pressure. A possible explanation is that the chemical pressure in ThMnPN plays a role similar to that of the physical one in LaMnPO, leaving the system on the verge of a metal-to-insulator transition. However, we note that the shrinkage of the cell volume for LaMnPO reaches ~17% at 20 GPa,[28] far exceeding the volume difference between LaMnPO and ThMnPN (3.15%, shown in Table 2). This may suggest that the effect of the physical and chemical pressure cannot be fully described by the change of the cell volume alone. Additional parameters, such as the bond length and bond angle, should be taken into account.

Besides, the magnetic structure under the physical or chemical pressure is another interesting issue. On the one hand, sophisticated high-pressure experiments on the magnetic susceptibility show that the antiferromagnetic transition in LaMnPO (manifested by the peak on the $\chi'-T$ curves) is suppressed to below 1.5 K at 34 GPa.[27] On the other hand, we observed similar susceptibility peaks at the T^* values in ThMnPnN, above which the antiferromagnetic state is still valid. This may suggest that the physical pressure effect on the magnetic exchange (which is sensitive to the distortion of the Mn coordination tetrahedra) is quite different from that of the chemical pressure. Otherwise, the possibility of an antiferromagnetic-to-antiferromagnetic phase transition in pressurized LnMnPnO should also be considered.

CONCLUSIONS

In conclusion, we have synthesized two new 1111-type Mn-based pnictides ThMnPnN (Pn = P, As). By comparing the crystal structure of the related compounds containing Th_2N_2 or La_2O_2 layers, we conclude that the internal chemical pressure commonly exists in the Th_2N_2 layer containing 1111-type compounds. The built-in chemical pressure plays a role similar to that of an external physical pressure, which accounts for the enhanced conductivity as well as the nonzero Sommerfeld coefficient. In addition, magnetic measurement reveals a second antiferromagnetic transition at low temperatures for both compounds. The exceptional properties make ThMnPnN new members for studying the mechanism of internal chemical pressure in 1111-type compounds. Further experimental and theoretical works are highly needed to clarify the precise magnetic structure and the mechanism of the chemical pressure.

ASSOCIATED CONTENT

Supporting Information

The Supporting Information is available free of charge at https://pubs.acs.org/doi/10.1021/acs.inorgchem.9b03294.

Magnetic structure refinement with different canting models (PDF)

Accession Codes

CCDC 1917536 and 1917554 contain the supplementary crystallographic data for this paper. These data can be obtained free of charge via www.ccdc.cam.ac.uk/data_request/cif, or by emailing data_request@ccdc.cam.ac.uk, or by contacting The Cambridge Crystallographic Data Centre, 12 Union Road, Cambridge CB2 1EZ, UK; fax: +44 1223 336033.

AUTHOR INFORMATION

Corresponding Authors

Yuxue Mei – *School of Physics & Optoelectronic Engineering, Shandong University of Technology, Zibo 255000, P. R. China*; Email: yuxue_mei@126.com

Cao Wang – *School of Physics & Optoelectronic Engineering, Shandong University of Technology, Zibo 255000, P. R. China*; orcid.org/0000-0001-9319-4737; Email: wangcao@sdut.edu.cn

https://dx.doi.org/10.1021/acs.inorgchem.9b03294
Inorg. Chem. 2020, 59, 2937–2944

Authors

Fuxiang Zhang − *School of Physics & Optoelectronic Engineering, Shandong University of Technology, Zibo 255000, P. R. China*

Baizhuo Li − *Department of Physics, Zhejiang University, Hangzhou 310027, P. R. China*

Qingyong Ren − *School of Physics and Astronomy, Shanghai Jiao Tong University, Shanghai 200240, P. R. China;* orcid.org/0000-0002-3163-9320

Huican Mao − *Department of Physics and Center for Advanced Quantum Studies, Beijing Normal University, Beijing 100875, P. R. China; Beijing National Laboratory for Condensed Matter Physics, Institute of Physics, Chinese Academy of Sciences, Beijing 100190, P. R. China*

Yuanhua Xia − *Key Laboratory of Neutron Physics, Institute of Nuclear Physics and Chemistry, China Academy of Engineering Physics, Mianyang 621999, P. R. China*

Bingfeng Hu − *Key Laboratory of Neutron Physics, Institute of Nuclear Physics and Chemistry, China Academy of Engineering Physics, Mianyang 621999, P. R. China*

Zichen Liu − *School of Physics & Optoelectronic Engineering, Shandong University of Technology, Zibo 255000, P. R. China*

Zhicheng Wang − *Department of Physics, Zhejiang University, Hangzhou 310027, P. R. China*

Yeting Shao − *Department of Physics, Zhejiang University, Hangzhou 310027, P. R. China*

Zhifa Feng − *School of Physics & Optoelectronic Engineering, Shandong University of Technology, Zibo 255000, P. R. China*

Shugang Tan − *School of Physics & Optoelectronic Engineering, Shandong University of Technology, Zibo 255000, P. R. China*

Yuping Sun − *School of Physics & Optoelectronic Engineering, Shandong University of Technology, Zibo 255000, P. R. China;* orcid.org/0000-0002-1330-0155

Zhi Ren − *Institute for Natural Sciences, Westlake Institute for Advanced Study, Hangzhou 310027, P. R. China*

Qiang Jing − *School of Physics & Optoelectronic Engineering, Shandong University of Technology, Zibo 255000, P. R. China*

Bo Liu − *School of Physics & Optoelectronic Engineering, Shandong University of Technology, Zibo 255000, P. R. China*

Huiqian Luo − *Beijing National Laboratory for Condensed Matter Physics, Institute of Physics, Chinese Academy of Sciences, Beijing 100190, P. R. China*

Jie Ma − *School of Physics and Astronomy, Shanghai Jiao Tong University, Shanghai 200240, P. R. China*

Guang-Han Cao − *Department of Physics, Zhejiang University, Hangzhou 310027, P. R. China;* orcid.org/0000-0002-9669-5761

Complete contact information is available at: https://pubs.acs.org/10.1021/acs.inorgchem.9b03294

Author Contributions

The manuscript was written through the contributions of all authors. All authors have given approval to the final version of the manuscript.

Notes

The authors declare no competing financial interest.

■ ACKNOWLEDGMENTS

This work was supported by the Natural Science Foundation of China (Grants 11304183, 11822411, 11961160699, 11804194, and U1732154), National Key Research and Development Program of China (Grants 2017YFA0303002, 2017YFA0303103, and 2018YFA0704201), Natural Science Foundation of Shandong Province (Grants ZR2019MA036 and ZR2016AQ08), and Project of Shandong Province Higher Educational Science and Technology Program (Grant J17KA183). Also, we thank Wei Liu from Hengderui Polyurethane Co., Ltd., for his kind contribution.

■ REFERENCES

(1) Kamihara, Y.; Watanabe, T.; Hirano, M.; Hosono, H. Iron-Based Layered Superconductor La[$O_{1-x}F_x$]FeAs (x = 0.05−0.12) with Tc = 26 K. *J. Am. Chem. Soc.* **2008**, *130*, 3296−3297.

(2) Pöttgen, R.; Johrendt, D. Materials with ZrCuSiAs Type Structure. *Z. Naturforsch., B: J. Chem. Sci.* **2008**, *63*, 1135−1148.

(3) Ozawa, T. C.; Kauzlarich, S. M. Chemistry of layered d-metal pnictide oxides and their potential as candidates for new superconductors. *Sci. Technol. Adv. Mater.* **2008**, *9*, 033003.

(4) Muir, S.; Subramanian, M. A. ZrCuSiAs type layered oxypnictides: A bird's eye view of LnM*Pn*O compositions. *Prog. Solid State Chem.* **2012**, *40*, 41−56.

(5) Ishida, K.; Nakai, Y.; Hosono, H. To What Extent Iron-Pnictide New Superconductors Have Been Clarified: A Progress Report. *J. Phys. Soc. Jpn.* **2009**, *78*, 062001.

(6) Ren, Z. A; Zhao, Z. X. Research and Prospects of Iron-Based Superconductors. *Adv. Mater.* **2009**, *21*, 4584−4592.

(7) Klimczuk, T.; Walker, H. C.; Springell, R.; Shick, A. B.; Hill, A. H.; Gaczyński, P.; Gofryk, K.; Kimber, S. A. J.; Ritter, C.; Colineau, E.; Griveau, J. -C.; Bouëxière, D.; Eloirdi, R.; Cava, R. J.; Caciuffo, R. Negative thermal expansion and antiferromagnetism in the actinide oxypnictide NpFeAsO. *Phys. Rev. B: Condens. Matter Mater. Phys.* **2012**, *85*, 174506.

(8) Klimczuk, T.; Shick, A. B.; Springell, R.; Walker, H. C.; Hill, A. H.; Colineau, E.; Griveau, J. -C.; Bouëxière, D.; Eloirdi, R.; Caciuffo, R. Bulk properties and electronic structure of PuFeAsO. *Phys. Rev. B: Condens. Matter Mater. Phys.* **2012**, *86*, 174510.

(9) Cheng, P.; Shen, B.; Mu, G.; Zhu, X. Y.; Han, F.; Zeng, B.; Wen, H. H. High-Tc superconductivity induced by doping rare-earth elements into CaFeAsF. *Europhys. Lett.* **2009**, *85*, 67003.

(10) Zhu, X.; Han, F.; Cheng, P.; Mu, G.; Shen, B.; Zeng, B.; Wen, H. H. Parent phase and superconductors in the fluorine derivative family. *Phys. C* **2009**, *469*, 381−384.

(11) Muraba, Y.; Matsuishi, S.; Hosono, H. La-Substituted CaFeAsH Superconductor with T_c = 47 K. *J. Phys. Soc. Jpn.* **2014**, *83*, 033705.

(12) Park, S. W.; Mizoguchi, H.; Kodama, K.; Shamoto, S.; Otomo, T.; Matsuishi, S.; Kamiya, T.; Hosono, H. Magnetic structure and electromagnetic properties of *Ln*CrAsO with a ZrCuSiAs-type structure (*Ln* = La, Ce, Pr, and Nd). *Inorg. Chem.* **2013**, *52*, 13363−13368.

(13) McGuire, M. A.; Garlea, V. O. Short-and long-range magnetic order in LaMnAsO. *Phys. Rev. B: Condens. Matter Mater. Phys.* **2016**, *93*, 054404 and references cited therein.

(14) Yanagi, H.; Kawamura, R.; Kamiya, T.; Kamihara, Y.; Hirano, M.; Nakamura, T.; Osawa, H.; Hosono, H. Itinerant ferromagnetism in the layered crystals LaCoO*X* (*X* = P, As). *Phys. Rev. B: Condens. Matter Mater. Phys.* **2008**, *77*, 224431.

(15) Ohta, H.; Yoshimura, K. Magnetic properties of *L*CoAsO (*L* = La−Gd). *Phys. Rev. B: Condens. Matter Mater. Phys.* **2009**, *80*, 184409.

(16) Pal, A.; Mehdi, S. S.; Husain, M.; Gahtori, B.; Awana, V. P. S. Complex magnetism and magnetotransport of *RE*CoPO (*RE* = La, Nd, and Sm). *J. Appl. Phys.* **2011**, *110*, 103913.

(17) Prando, G.; Bonfà, P.; Profeta, G.; Khasanov, R.; Bernardini, F.; Mazzani, M.; Brüning, E. M.; Pal, A.; Awana, V. P. S.; Grafe, H. -J.; Büchner, B.; De Renzi, R.; Carretta, P.; Sanna, S. Common effect of chemical and external pressures on the magnetic properties of *R*CoPO (*R* = La, Pr). *Phys. Rev. B: Condens. Matter Mater. Phys.* **2013**, *87*, 064401.

(18) Watanabe, T.; Yanagi, H.; Kamihara, Y.; Kamiya, T.; Hirano, M.; Hosono, H. Nickel-based layered superconductor, LaNiOAs. *J. Solid State Chem.* **2008**, *181*, 2117−2120.
(19) Watanabe, T.; Yanagi, H.; Kamiya, T.; Kamihara, Y.; Hiramatsu, H.; Hirano, M.; Hosono, H. Nickel-Based Oxyphosphide Superconductor with a Layered Crystal Structure, LaNiOP. *Inorg. Chem.* **2007**, *46*, 7719−7721.
(20) Marcinkova, A.; Hansen, T. C.; Curfs, C.; Margadonna, S.; Bos, J. -W. G. Nd-induced Mn spin-reorientation transition in NdMnAsO. *Phys. Rev. B: Condens. Matter Mater. Phys.* **2010**, *82*, 174438.
(21) Corkett, A. J.; Free, D. G.; Clarke, S. J. Spin-Reorientation Transition in CeMnAsO. *Inorg. Chem.* **2015**, *54*, 1178−1184.
(22) Kimber, S. A. J.; Hill, A. H.; Zhang, Y. Z.; Jeschke, H. O.; Valentí, R.; Ritter, C.; Schellenberg, I.; Hermes, W.; Pöttgen, R.; Argyriou, D. N. Local moments and symmetry breaking in metallic PrMnSbO. *Phys. Rev. B: Condens. Matter Mater. Phys.* **2010**, *82*, 100412.
(23) Sun, Y. L.; Bao, J. K.; Luo, Y. K.; Feng, C. M.; Xu, Z. A.; Cao, G. H. Insulator-to-metal transition and large thermoelectric effect in $La_{1-x}Sr_xMnAsO$. *Europhys. Lett.* **2012**, *98*, 17009.
(24) Hanna, T.; Matsuishi, S.; Kodama, K.; Otomo, T.; Shamoto, S.; Hosono, H. From antiferromagnetic insulator to ferromagnetic metal: Effects of hydrogen substitution in LaMnAsO. *Phys. Rev. B: Condens. Matter Mater. Phys.* **2013**, *87*, 020401.
(25) Saparov, B.; Singh, D. J.; Garlea, V. O.; Sefat, A. S. Crystal, magnetic, and electronic structures, and properties of new BaMn*Pn*F (*Pn* = As, Sb, Bi). *Sci. Rep.* **2013**, *3*, 2154.
(26) Yanagi, H.; Watanabe, T.; Kodama, K.; Iikubo, S.; Shamoto, S.; Kamiya, T.; Hirano, M.; Hosono, H. Antiferromagnetic bipolar semiconductor LaMnPO with ZrCuSiAs-type structure. *J. Appl. Phys.* **2009**, *105*, 093916.
(27) Guo, J.; Simonson, J. W.; Sun, L.; Wu, Q.; Gao, P.; Zhang, C.; Gu, D.; Kotliar, G.; Aronson, M.; Zhao, Z. Observation of antiferromagnetic order collapse in the pressurized insulator LaMnPO. *Sci. Rep.* **2013**, *3*, 2555.
(28) Simonson, J. W.; Yin, Z. P.; Pezzoli, M.; Guo, J.; Liu, J.; Post, K.; Efimenko, A.; Hollmann, N.; Hu, Z.; Lin, H.-J.; Chen, C.-T.; Marques, C.; Leyva, V.; Smith, G. J.; Lynn, W.; Sun, L. L.; Kotliar, G.; Basov, D. N.; Tjeng, L. H.; Aronson, M. C. From antiferromagnetic insulator to correlated metal in pressurized and doped LaMnPO. *Proc. Natl. Acad. Sci. U. S. A.* **2012**, *109*, E1815−E1819.
(29) Wang, C.; Wang, Z. C.; Mei, Y. X.; Li, Y. K.; Li, L.; Tang, Z. T.; Liu, Y.; Zhang, P.; Zhai, H. F.; Xu, Z. A.; Cao, G. H. A New ZrCuSiAs-Type Superconductor: ThFeAsN. *J. Am. Chem. Soc.* **2016**, *138*, 2170−2173.
(30) Wang, G.; Shi, X. Electronic structure and magnetism of ThFeAsN. *Europhys. Lett.* **2016**, *113*, 67006.
(31) Singh, D. J. ThFeAsN in relation to other iron-based superconductors. *J. Alloys Compd.* **2016**, *687*, 786−789.
(32) Albedah, A.; Nejadsattari, F.; Stadnik, Z. M.; Wang, Z. C.; Wang, C.; Cao, G. H. Absence of the stripe antiferromagnetic order in the new 30 K superconductor ThFeAsN. *J. Alloys Compd.* **2017**, *695*, 1128−1136.
(33) Mao, H. C.; Wang, C.; Maynard-Casely, H. E.; Huang, Q. Z.; Wang, Z. C.; Cao, G. H.; Li, S. L.; Luo, H. Q. Neutron powder diffraction study on the iron-based nitride superconductor ThFeAsN. *Europhys. Lett.* **2017**, *117*, 57005.
(34) Shiroka, T.; Shang, T.; Wang, C.; Cao, G. H.; Eremin, I.; Ott, H. R.; Mesot, J. High-Tc superconductivity in undoped ThFeAsN. *Nat. Commun.* **2017**, *8*, 156.
(35) Adroja, D.; Bhattacharyya, A.; Biswas, P. K.; Smidman, M.; Hillier, A. D.; Mao, H. C.; Luo, H. Q.; Cao, G. H.; Wang, Z. C.; Wang, C. Multigap superconductivity in ThAsFeN investigated using μSR measurements. *Phys. Rev. B: Condens. Matter Mater. Phys.* **2017**, *96*, 144502.
(36) Wang, Z. C.; Shao, Y. T.; Wang, C.; Wang, Z.; Xu, Z. A.; Cao, G. H. Enhanced superconductivity in ThNiAsN. *Europhys. Lett.* **2017**, *118*, 57004.
(37) Rodríguez-Carvajal, J. Recent advances in magnetic structure determination by neutron powder diffraction. *Phys. B* **1993**, *192*, 55−69.
(38) Johnston, D. C.; McQueeney, R. J.; Lake, B.; Honecker, A.; Zhitomirsky, M. E.; Nath, R.; Furukawa, Y.; Antropov, V. P.; Singh, Y. Magnetic exchange interactions in $BaMn_2As_2$: A case study of the J_1-J_2-J_c Heisenberg model. *Phys. Rev. B: Condens. Matter Mater. Phys.* **2011**, *84*, 094445.
(39) Wildman, E. J.; Emery, N.; Mclaughlin, A. C. Electronic and magnetic properties of $Nd_{1-x}Sr_xMnAsO$ oxyarsenides. *Phys. Rev. B: Condens. Matter Mater. Phys.* **2014**, *90*, 224413.
(40) Emery, N.; Wildman, E. J.; Skakle, J. M. S.; Giriat, G.; Smith, R. I.; Mclaughlin, A. C. Giant magnetoresistance in oxypnictides (La,Nd)OMnAs. *Chem. Commun.* **2010**, *46*, 6777−6779.
(41) Wildman, E. J.; Sher, F.; Mclaughlin, A. C. Absence of Colossal Magnetoresistance in the Oxypnictide $PrMnAsO_{0.95}F_{0.05}$. *Inorg. Chem.* **2015**, *54*, 2536−2542.

https://dx.doi.org/10.1021/acs.inorgchem.9b03294
Inorg. Chem. 2020, 59, 2937−2944